Fermi surface studies of the topologically nontrivial compound YSi

Vikas Saini, Souvik Sasmal, Ruta Kulkarni, Bahadur Singh,* and A. Thamizhavel†
Department of Condensed Matter Physics and Materials Science, Tata Institute of Fundamental Research, Homi Bhabha Road, Colaba, Mumbai 400005, India

(Received 10 February 2021; accepted 10 May 2021; published 25 May 2021)

The Fermi surface properties of the nontrivial system YSi are investigated by de Haas–van Alphen (dHvA) oscillation measurements combined with the first-principles calculations. Three main frequencies (α, β, γ) are probed up to a magnetic field of 14 T in dHvA oscillations. The α branch possesses nontrivial topological character with a Berry phase of 0.52π for $B \parallel [100]$ and 1.39π for $B \parallel [001]$ direction. The linear dispersion of α branch along Γ to Z direction corroborates the light mass of charge carriers. The effective mass of α branch is estimated to be $0.069\ m_e$ for $B \parallel [100]$, with third-lowest Landau level ($n = 2$) up to 14 T. The γ pocket of 295 T frequency exhibits two-dimensional character and a high Fermi velocity of 6.7×10^5 m s^{-1}. The band structure calculations reveal multiple nodal crossings in the vicinity of Fermi energy E_F without spin-orbit coupling (SOC). Inclusion of SOC opens a small gap at the nodal crossings and results in nonsymmorphic symmetry enforced Dirac points at some high symmetry points, suggesting YSi is a symmetry enforced topological metal.

DOI: 10.1103/PhysRevB.103.195154

I. INTRODUCTION

Topological semimetals have gained significant attention on both theoretical and experimental fronts in recent years owing to their exotic properties. They exhibit symmetry protected bulk and surface states which results in novel phenomena and transport properties with tremendous potential for applications in quantum technologies and energy sciences [1–6]. Topological semimetals can be classified based on the dimensionality and degeneracy of the crossing points. In particular, topological Dirac semimetal has zero-dimensional fourfold degenerate crossing points in the vicinity of Fermi energy (E_F) with low-energy excitations as Dirac fermions. These fermions constitute linear energy dispersion that leads to observed exotic phenomenon in the electrical transport measurements. The fourfold degeneracy of the Dirac point is ensured by the presence of both the time-reversal $\mathcal{T}$ and inversion $\mathcal{I}$ symmetries along with specific crystalline symmetries. This fourfold degeneracy is lifted by breaking either inversion or time-reversal symmetries, transitioning Dirac semimetals (DSM) to Weyl semimetals (WSM) with twofold Weyl nodal crossings [7–10]. Cd_3As_2 and Na_3Bi are known prototype topological Dirac semimetals, which were predicted theoretically and realized in experiments. They exhibit ultrahigh mobility, extremely high magnetoresistance, and show exotic phenomena such as chiral anomaly, quantum Hall effect, among others owing to symmetry protected Dirac band crossings. The extensive studies of Shubnikov–de Haas (SdH) and de Haas–van Alphen (dHvA) oscillations confirmed topological nontrivial nature of these compounds from the Berry phase analysis and other unusual properties [8,9,11–16].

In view of finding new topological semimetals, we investigate the Fermi surface and topological properties of binary compound YSi by de Haas–van Alphen (dHvA) oscillations and first-principles calculations. We have chosen YSi for the present investigation as it crystallizes in the space group *Cmcm* which is a nonsymmorphic space group and hence possesses high possibility for being a Dirac semimetal. Furthermore, there are no previous studies on YSi except for the crystal structure [17] and a recent theoretical investigation by Li *et al.* [18] on the structural stability of YSi. We have synthesized a high-quality single-crystal YSi by the Czochralski method. From dHvA quantum oscillations studies, YSi is found to possess nontrivial Fermi pockets. Three different branches (α, β, and γ) are probed up to a magnetic field of 14 T. The nontrivial α pocket is observed for the magnetic field along all three directions with a subtle variation in the frequency, implying a nonuniform cross section of the Fermi surface suggesting an anisotropic nature of the α pocket. In contrast, β and γ pockets are observed only for $B \parallel [010]$ direction, suggesting a two-dimensional (2D) nature of the Fermi surface in agreement with our first-principles results. These pockets show trivial band character. The detailed band structure analysis shows that both the valence and conduction bands participate in the formation of the Fermi surface with the hole and electron pockets. The type-I nodal antiband crossing along the Γ-Z direction in the vicinity of Fermi energy leads to the nontrivial α pocket.

II. METHODS

From the binary phase diagram of Y and Si, it is obvious that YSi melts congruently at 1845 °C [19] and hence can be grown directly from its melt. A tetra-arc furnace has been used to grow the single crystal of YSi by the Czochralski method. High purity starting materials of Y (3N pure, Alfa-Aesar) and Si (5N pure, Alfa-Aesar) were taken in the ratio of 1 : 1.05

*bahadur.singh@tifr.res.in
†thamizh@tifr.res.in

 ©2021 American Physical Society

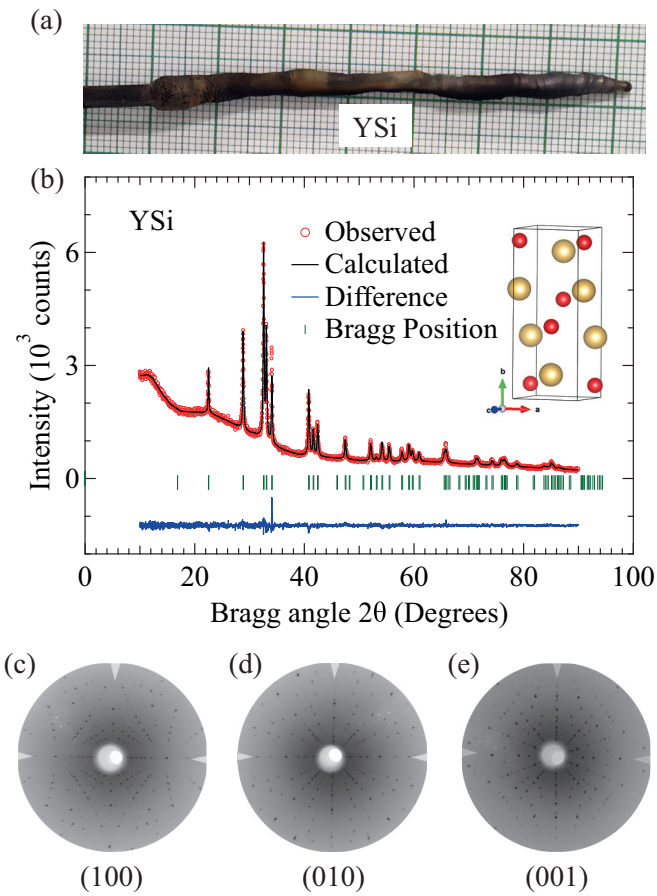

FIG. 1. (a) As grown single crystalline pulled ingot. (b) Room temperature powder x-ray diffraction and structural refinement by Rietveld method. The inset shows the crystal structure of YSi with *b* as the longest axis. The large (yellow) and small (red) balls identify Y and Si atoms, respectively. (c), (d), and (e) The observed Laue diffraction pattern along the three principal crystallographic planes (100), (010), and (001), respectively.

and repeatedly melted to make a homogenous polycrystalline ingot of about 8 to 10 g. A seed crystal was cut from this polycrystalline ingot to grow the single crystal in a vacuum chamber filled with Ar gas. The polycrystalline ingot was melted and the seed crystal was slowly inserted into the melt and pulled very rapidly to start with. Once the steady-state condition is achieved, the pulling rate was maintained at 10 mm/h. The as grown pulled ingot had a diameter ≈4 mm and length ≈70 mm and is shown in Fig. 1(a). The composition analysis was performed using energy dispersive analysis by x-rays (EDAX). A small portion of the crystal was crushed to a fine powder and subjected to room temperature powder x-ray diffraction (XRD) measurement in a PANalytical x-ray diffractometer equipped with a monochromatic Cu-K_α source with the wavelength $\lambda = 1.5406$ Å. To confirm the single-crystalline nature of the sample and to orient and cut the crystal along the three principal crystallographic directions we have performed Laue diffraction in the back reflection geometry. The oriented crystal was cut into a rectangular bar shape using a spark erosion cutting machine. Magnetic measurements were performed in a vibrating sample magnetometer (VSM) (PPMS, Quantum Design, USA) down to 2 K and in a magnetic field of 14 T.

Band structure calculations were carried out with the projector augmented wave (PAW) method [20] within the density functional theory (DFT) [21] framework as implemented in the Vienna *ab initio* simulation package (VASP) [22,23]. The exchange-correlation effects were considered with the generalized gradient approximation (GGA) with the Perdew, Burke, and Ernzerhof parametrization [24]. The spin-orbit coupling (SOC) was included self-consistently. An energy cutoff of 310 eV was used for the plane-wave basis set and a 11 × 11 × 13 Γ-centered *k* mesh was used for the bulk Brillouin zone sampling. The Xcrysden program was used to visualize the Fermi surface [25]. The robustness of results is further verified by calculating electronic properties using the WIEN2K code, which considers a full-potential linearized augmented plane-wave formalism [26]. The quantum oscillations calculation was performed using the SKEAF code [27].

III. RESULTS AND DISCUSSION

A. Crystal structure

We start discussing the crystal structure of our grown single crystals of YSi. The phase purity of the grown crystal was analyzed by powder XRD measurement. It has been reported that YSi crystallizes in the centrosymmetric orthorhombic crystal structure with space group *Cmcm* (No. 63) [17]. The unit cell structure of YSi is shown in the inset of Fig. 1(b). The powder XRD pattern is shown in Fig. 1(b) and it is evident that there are no discernible impurity peaks in the entire 2θ range from 10° to 90°. From the Rietveld analysis using FULLPROF software [28] we confirmed that this compound crystallizes in the *Cmcm* space group. The obtained lattice parameters from the Rietveld analysis, $a = 4.260$ Å, $b = 10.530$ Å, and $c = 3.830$ Å, are found to be in close agreement with the published data [17]. The Y and Si atoms occupy 4*c* Wyckoff position with coordinates (0, 0.3598, 0.25) and (0, 0.0764, 0.25), respectively. The Laue diffraction pattern attests good quality of the grown crystal as shown in Figs. 1(c), 1(d), and 1(e), respectively, for (100), (010), and (001) planes.

B. Electronic structure

Figure 2(a) shows the bulk Brillouin zone for the primitive crystal structure of YSi, where high-symmetry points are marked explicitly. The calculated bulk band structure of YSi along various high-symmetry directions without SOC is shown in Fig. 2(b). It is seen to be metallic where various bands cross the Fermi level. Importantly, many symmetry protected spinless band crossings are found along the high-symmetry lines such as *R*-*Z* and *T*-*Z* at the Brillouin zone boundaries as well at the generic *k* points. Along the Γ-*Z* direction three bands cross, forming both the type-I and type-II nodal crossings as shown in Fig. 2(e). The orbital resolved band structure shows that these band crossings are composed of Y *d* and Si *p* orbitals [Fig. 2(d)]. The structure with SOC is shown in Figs. 2(c) and 2(f). The various nodal crossings at the generic *k* points are gapped. However, owing to the presence of screw rotations $\{C_{2z}|00\frac{1}{2}\}$ and $\{C_{2y}|00\frac{1}{2}\}$ and glide mirror $\{M_y|00\frac{1}{2}\}$, the band crossings at *R*, *Z*, and *T* points

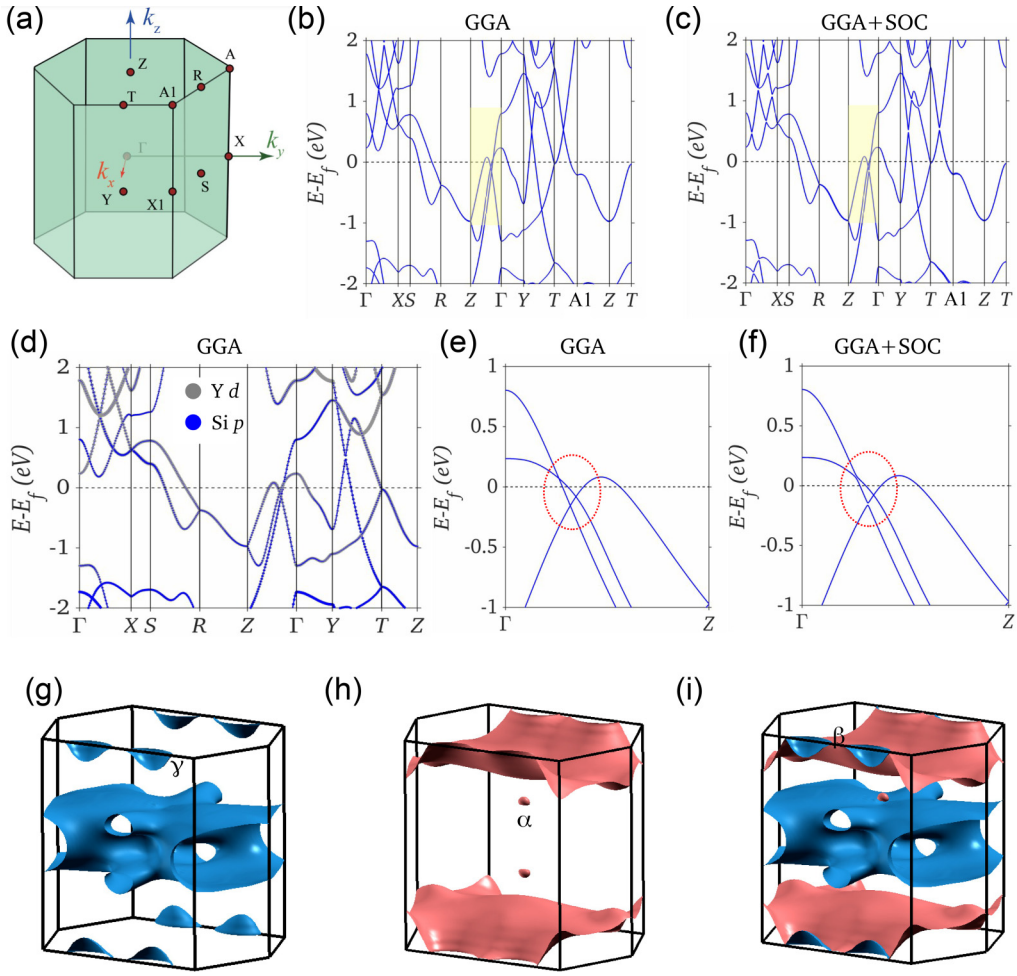

FIG. 2. (a) Bulk Brillouin zone of orthorhombic YSi. The high-symmetry points are marked. Bulk band structure of YSi (b) without and (c) with spin-orbit coupling (SOC). (d) Orbital resolved band structure without SOC. Y d and Si p states are shown with gray and blue markers, respectively. (e) and (f) Close up of the bands along Γ-Z direction in the area highlighted by yellow rectangles in (b) and (c). The broken circles highlight the three crossing bands. The crossing bands are gapped in the presence of SOC. (g) and (h) The calculated individual Fermi pockets and (i) the Fermi surface of YSi.

remain protected, forming high symmetry point Dirac states. Notably, YSi is a filling enforced nonsymmorphic topological metal with $4n+2$; $n=7$ electrons/unit cell without disconnected valence and conduction bands in k space. Since all states in a nonsymmorphic system come in a pair of four bands, a clear gap does not exist for $4n+2$ (n is a positive integer) electrons/unit cell and thus, the Z_2 topological number is not defined for pristine YSi [29]. However, we find that the electron or hole doping with 2 electrons/unit cell leads to a Z_2 topological metallic state with $Z_2 = (1;000)$ in YSi.

The calculated bulk Fermi surface of YSi is shown in Fig. 2(i), whereas its constituent individual pockets are illustrated in Figs. 2(g) and 2(h). Owing to the multiband crossings at the Fermi level, the Fermi surface is composed of both the electron and hole bands. We mark a small pocket along the Γ-Z direction as α which is formed by bands highlighted in the broken red circle in Fig. 2(f). On the other hand, the pocket along the T-$A1$ direction is identified as γ. Additionally, giant Fermi pockets are enclosing Γ and Z points. The calculated quantum oscillation frequencies are summarized in Table I. It is found that a shift of $\sim +11$ meV in the Fermi level is essential to reproduce the experimentally observed frequencies. Such shifts in Fermi energy with respect to the computed band structures are essential to consider the effects of crystal doping/imperfections in experiments and are commonly invoked in the literature [30]. The observed oscillations of the α pocket are observed in all three directions and it carries the lowest frequency of 21 T for $B \parallel [100]$. β pocket is observed only for $B \parallel [010]$ and has a frequency of 61 T. Also, the γ pocket is observed when $B \parallel [010]$ with a high frequency of 295 T. These oscillations are well captured in our first-principles results (see below for more details).

C. de Haas–van Alphen quantum oscillations studies

The field dependence of the magnetization measured in a VSM at 2 K, up to a field of 14 T, along the three principal crystallographic directions is shown in Figs. 3(a)–3(c). Robust dHvA oscillations are observed along all three directions. Long-period oscillations are observed for $B \parallel [100]$ and [001] directions, while for [010] direction strong oscillations with

TABLE I. Quantum parameters estimated from dHvA oscillations, $F_{\rm expt}$ and $F_{\rm calc}$ are the experimental and calculated dHvA frequencies; $m^*_{\rm expt}$ and $m^*_{\rm calc}$ are the experimental and calculated effective masses; τ_q is the quantum relaxation time; μ_q is the quantum mobility, $k_{\rm F}$ is the Fermi wave vector, $v_{\rm F}$ is the Fermi velocity, $E_{\rm F}$ is the Fermi level, l_q is the mean free path, and n is the carrier density.

Field direction	$F_{\rm expt}$ (T)	$F_{\rm calc}$ (T)	$m^*_{\rm expt}$ (m_e)	$m^*_{\rm calc}$ (m_e)	τ_q (10^{-13} s)	μ_q (cm^2 V^{-1} s^{-1})	$k_{\rm F}$ (Å^{-1})	$v_{\rm F}$ (10^5 m/s)	$E_{\rm F}$ (meV)	l_q (nm)	n
[100]	21 (α)	21.8	0.069(1)	0.082			0.025	4.26	71.2		5.56×10^{17} cm^{-3}
[010]	295 (γ)	294.7	0.162(2)	0.147	2.2	2384	0.095	6.75	421	148.65	7.14×10^{12} cm^{-2}
	61 (β)	71.5	0.097(2)	0.162	1.14	2053	0.043	5.1	145	58.39	1.48×10^{12} cm^{-2}
[001]	34 (α)	28.1	0.096(4)	0.095	2.15	3927	0.032	3.85	81.1	82.77	1.109×10^{18} cm^{-3}

multiple frequencies are observed. At 2 K the oscillations begin to appear from 2 T field and this corresponds to the magnetic length $l_{\rm B} = \sqrt{\frac{\hbar}{eB}} \approx 18$ nm thus indicating a good quality of the grown single crystal. As the temperature is increased, the amplitudes of the dHvA oscillations tend to decrease and are not discernible for a temperature greater than 21 K. The nonoscillatory background data were subtracted to extract the dHvA oscillation frequency by fast Fourier transform (FFT). The FFT spectra at $T = 2$ K along the three principal crystallographic directions are shown in Figs. 3(d)–3(f). When the magnetic field is along the [100] direction, a single fundamental frequency at 21 T has been observed which is named as α. For $B \parallel [010]$ three fundamental frequencies have been observed at 36 T (α), 61 T (β), and 295 T (γ) with the second harmonic at 590 T (2γ), while for $B \parallel [001]$ a single frequency at 34 T (α) and its corresponding second harmonic was observed at 68 T (2α). It is to be mentioned here that the α branch is observed along all three directions with a subtle anisotropy in the frequency thus representing a small anisotropic three-dimensional (3D) Fermi surface.

We have estimated the quantum parameters by analyzing the frequency spectrum of the observed oscillations. The temperature dependence of the FFT amplitude of the three fundamental frequencies for $B \parallel [010]$ is shown in Fig. 4(a). The amplitude of the frequencies decreases as the temperature increases. The T dependence of the amplitude of the oscillation frequencies are shown Fig. 4(b) and fitted to thermal damping factor of Lifshitz-Kosevich expression: $R_T = (X/\sinh X)$, where $X = (\lambda T m^*/B)$, $\lambda = (2\pi^2 k_B m_e/e\hbar)$ (=14.69 T), and m^* is the cyclotron effective mass of the charge carriers which is expressed in units of free electron mass m_e [5,31,32]. The calculated effective masses for the various frequencies are listed in Table I. It is evident from the table that the effective masses of charge carriers are

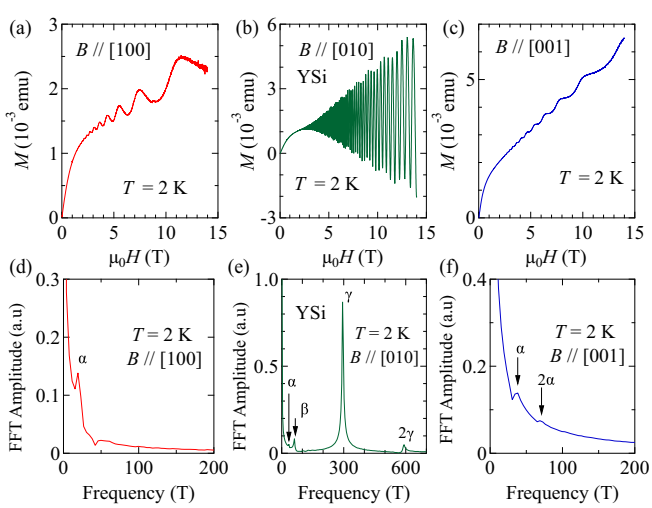

FIG. 3. (a), (b), and (c) dHvA quantum oscillations observed along the three principal crystallographic directions in YSi at $T = 2$ K. (d), (e), and (f) The obtained FFT frequency spectrum. The α branch is observed along all the three directions while β and γ are observed only along the [010] direction.

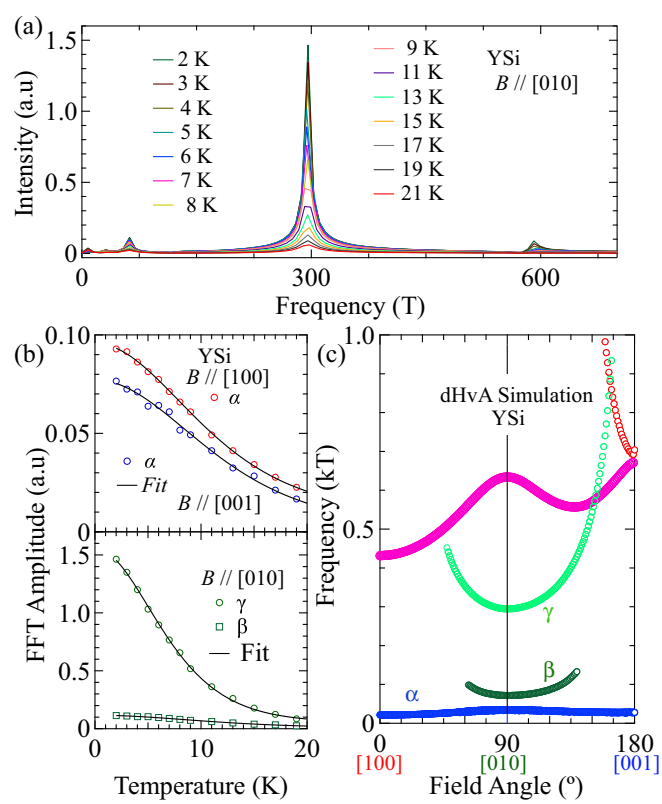

FIG. 4. (a) Temperature dependence of the FFT amplitude of the oscillation. The FFT amplitude decreases with increasing temperature. (b) Mass plot of the frequencies mentioned along the three principal crystallographic directions. The solid lines are the fits to the thermal damping factor of the Lifshitz-Kosevich expression (see text for details). (c) Calculated angular dependence of the dHvA oscillations for α, β, and γ Fermi pockets.

very small for all the observed main frequencies suggesting Dirac-like dispersion of bands and comparable to that of the gapless Dirac system Cd_3As_2 [33].

To understand the topological character of the charge carriers in YSi, we have performed the Berry phase analysis of the dHvA oscillations using the Lifshitz-Kosevich (L-K) formula [34,35] as given below,

$$\Delta M \propto -B^k R_T R_D R_s \sin\left[2\pi\left(\frac{F}{B}+\psi\right)\right], \qquad (1)$$

where R_T, R_D, and R_S are the thermal, magnetic field, and spin damping factors and ψ is the phase factor. The expression for R_T has already been defined while that for R_D is $R_D = \exp(-14.69 m^* T_D/B)$ where T_D is the Dingle temperature and $R_S = \cos(\pi g r m^*/2m_0)$, where g is the Landé g factor and r is the harmonic number. In Eq. (1) $k = 1/2$ for 3D Fermi surface while it is zero for 2D Fermi surface. The phase factor ψ is given by $\psi = [(\frac{1}{2} - \frac{\Phi_B}{2\pi}) - \delta]$, where δ is the additional phase factor which depends on the dimensionality of the Fermi surface. $\delta = 0$ for 2D Fermi surface and $\delta = \pm 1/8$ for 3D Fermi surface where the + sign corresponds to hole pocket and − sign corresponds to electron pocket.

For $B \parallel [010]$, two additional frequencies, viz., β and γ, are observed at 61 and 295 T which are absent in the other two directions, thus suggesting the anisotropic nature of the Fermi surface and 2D character of these two bands. This has been further verified in the quantum oscillations simulation for β and γ bands as shown in Fig. 4(c). For β band the oscillation frequency is minimum when the magnetic field is parallel to [010] direction and as the magnetic field is rotated from [010] to [100] and [001] directions, quantum oscillations disappear beyond 28° and 50°, respectively. Similarly, for γ band 295 T frequency is observed along [010] direction. When the magnetic field rotates further from [010] to [100] and [001] directions, quantum oscillations disappear beyond 47° and 67°, respectively. The disappearance of quantum oscillations for both bands, beyond certain angles, reveals the 2D character of these bands. Whereas the α band oscillation frequency is continuous and shows a small anisotropy as the field is rotated.

Using the Onsager's relation $F = \frac{\hbar}{2\pi e} A_F$, we have estimated the cross-sectional area for γ frequency as 0.028 Å^{-2}. To estimate the Dingle temperature T_D of the γ branch, we have used the band-pass filter to isolate the oscillations corresponding to the frequency 295 T and used the 2D L-K expression in the high magnetic field region as shown in Fig. 5(a). The reasonably good fit results in a Dingle temperature T_D of 5.52 K. A similar estimate to the Dingle temperature is made for the β pocket which gives $T_D = 10.62$ K. From the obtained values of m^* and T_D, we have estimated the quantum parameters for individual frequencies. The Fermi wave vector k_F is calculated using $(\frac{A_F}{\pi})^{1/2}$, where A_F is extremal cross section of the Fermi surface and obtained from the Onsager relation. We obtain Fermi velocity ($v_F = \frac{\hbar k_f}{m^*}$), quantum scattering time ($\tau_q = \frac{\hbar}{2\pi k_B T_D}$), and quantum mobility ($\mu_q = \frac{e\tau_q}{m^*}$). The surface carrier density n_{2D} and the volume carrier density n_{3D} is obtained by $\frac{k_F^2}{4\pi}$ and $\frac{k_F^3}{3\pi^2}$, respectively. The Fermi level ($E_F = m^* v_F^2$) for the three fundamental frequencies, quantum mean free path ($l_q = v_F \tau_q$), are also estimated as listed in

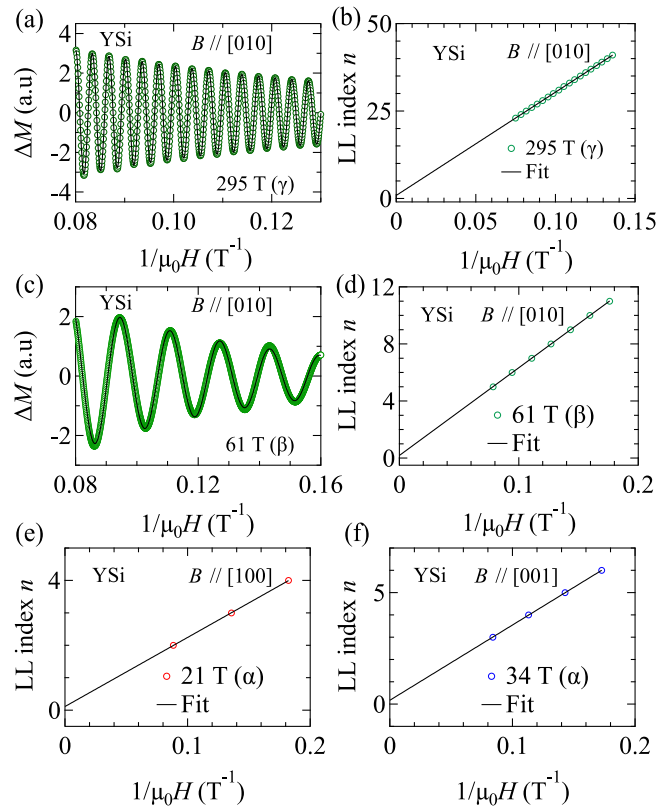

FIG. 5. (a) The band-pass filtered dHvA oscillations of the γ branch measured at $T = 2$ K for $B \parallel [010]$, the solid line corresponds to the L-K formula fitting. (b) LL-fan diagram corresponding to the γ branch. (c) L-K formula fitting of the filtered β-branch oscillations, (d) the LL-fan diagram corresponding to β branch. (e) and (f) LL-fan diagram of the α branch along the [100] and [001] directions.

Table I. We extract the information of the Berry phase of Fermi pockets by plotting the Landau level (LL) fan diagram. We assign the LL-index $n \pm \frac{1}{4}$ $(= F/B + \psi)$ to the maxima and minima of quantum oscillations, respectively, for + and − sign. For $B \parallel [010]$ there are multiple frequencies in the quantum oscillation, hence we have used the band-pass filtered oscillation to construct the LL-fan diagram where n is plotted as a function of the inverse magnetic field as shown in Figs. 5(b) and 5(d). The plots are straight lines and the slope corresponds to the oscillation frequency while the intercept gives the phase factor ψ mentioned in Eq. (1). For the γ branch, the intercept is 0.880(27), which gives a Berry phase (Φ_B) of -0.25π, revealing the trivial character of γ pocket. Similarly, the intercept for the β branch (61 T) is estimated to be 0.699(30), which corresponds to Φ_B of 0.1π and suggests a trivial nature of this pocket. The obtained intercept for α branch is 0.114(17) and 0.175(20) for $B \parallel [100]$ and $B \parallel [001]$ directions with $\Phi_B = 0.52\pi$ and 1.39π, respectively [see Figs. 5(e) and 5(f)]. This suggests a nontrivial nature of this Fermi pocket. Notably, the third-lowest Landau level for α branch has been achieved in a field of 14 T. It exhibits a small Fermi surface which is even smaller than the reported Fermi surfaces for Cd_3As_2 and ZrSiS systems [33,36].

IV. CONCLUSION

We have grown the single crystal of YSi using the Czochralski method. The band structure shows multiple nodal band crossings near the Fermi level. The Fermi surface is formed by both the electron and hole bands, resulting in multiple Fermi pockets with both small and large areas. Importantly, our calculated quantum oscillation frequencies match well with the observed frequencies. The dHvA oscillation measurements performed along the three principal crystallographic directions have revealed three Fermi pockets, namely α, β, and γ, in accord with our first-principles calculations. The α band obeys linear dispersion around the Fermi energy which results in a very small effective mass $0.069m_e$ for $B \parallel [100]$ direction, which is smaller than other well-known Dirac and Weyl semimetals [37–43]. The estimated Berry phase is 0.52π for $B \parallel [100]$ and 1.39π for $B \parallel [001]$ which refers to a nontrivial topological character and is observed along all the three principal directions with subtle anisotropy. The observed trivial Fermi pockets corresponding to the β and γ branches show a 2D character with quantum scattering time 1.14×10^{-13} and 2.2×10^{-13} s, respectively, which is of the same order as observed in ZrSiS and $PtBi_2$ systems [36,38]. The large quantum mean free path and high quantum mobility signifies the suppression of backscattering in YSi. These results make YSi an interesting topological material where nontrivial band crossings can be explored in angle-resolved photoemission spectroscopy (ARPES) and scanning tunneling microscopy (STM).

[1] A. Bansil, H. Lin, and T. Das, Rev. Mod. Phys. **88**, 021004 (2016).
[2] M. Z. Hasan and C. L. Kane, Rev. Mod. Phys. **82**, 3045 (2010).
[3] X.-L. Qi and S.-C. Zhang, Rev. Mod. Phys. **83**, 1057 (2011).
[4] M. Vergniory, L. Elcoro, C. Felser, N. Regnault, B. A. Bernevig, and Z. Wang, Nature (London) **566**, 480 (2019).
[5] J. Hu, S.-Y. Xu, N. Ni, and Z. Mao, Annu. Rev. Mater. Res. **49**, 207 (2019).
[6] L. Fu and C. L. Kane, Phys. Rev. B **76**, 045302 (2007).
[7] B. Singh, A. Sharma, H. Lin, M. Z. Hasan, R. Prasad, and A. Bansil, Phys. Rev. B **86**, 115208 (2012).
[8] Z. Wang, H. Weng, Q. Wu, X. Dai, and Z. Fang, Phys. Rev. B **88**, 125427 (2013).
[9] Z. Wang, Y. Sun, X.-Q. Chen, C. Franchini, G. Xu, H. Weng, X. Dai, and Z. Fang, Phys. Rev. B **85**, 195320 (2012).
[10] B. Lv, N. Xu, H. Weng, J. Ma, P. Richard, X. Huang, L. Zhao, G. Chen, C. Matt, F. Bisti *et al.*, Nat. Phys. **11**, 724 (2015).
[11] S.-Y. Xu, C. Liu, S. Kushwaha, T.-R. Chang, J. Krizan, R. Sankar, C. Polley, J. Adell, T. Balasubramanian, K. Miyamoto *et al.*, arXiv:1312.7624.
[12] C. Zhang, Y. Zhang, X. Yuan, S. Lu, J. Zhang, A. Narayan, Y. Liu, H. Zhang, Z. Ni, R. Liu *et al.*, Nature (London) **565**, 331 (2019).
[13] C. Zhang, E. Zhang, W. Wang, Y. Liu, Z.-G. Chen, S. Lu, S. Liang, J. Cao, X. Yuan, L. Tang *et al.*, Nat. Commun. **8**, 13741 (2017).
[14] S. K. Kushwaha, J. W. Krizan, B. E. Feldman, A. Gyenis, M. T. Randeria, J. Xiong, S.-Y. Xu, N. Alidoust, I. Belopolski, T. Liang *et al.*, APL Mater. **3**, 041504 (2015).
[15] C.-K. Chiu and A. P. Schnyder, J. Phys. Conf. Ser. **603**, 012002 (2015).
[16] T. Liang, Q. Gibson, M. N. Ali, M. Liu, R. Cava, and N. Ong, Nat. Mater. **14**, 280 (2015).
[17] E. Parthe, Acta Crystallogr. **12**, 559 (1959).
[18] J. Li, L. Zhang, Z.-H. Gao, S. Zhang, C. Lu, and G.-Q. Li, Struct. Chem. **27**, 983 (2016).
[19] T. Button, I. McColm, and J. Ward, J. Less-Common Met. **159**, 205 (1990).
[20] P. E. Blöchl, Phys. Rev. B **50**, 17953 (1994).
[21] P. Hohenberg and W. Kohn, Phys. Rev. **136**, B864 (1964).
[22] G. Kresse and D. Joubert, Phys. Rev. B **59**, 1758 (1999).
[23] G. Kresse and J. Furthmüller, Phys. Rev. B **54**, 11169 (1996).
[24] J. P. Perdew, K. Burke, and M. Ernzerhof, Phys. Rev. Lett. **77**, 3865 (1996).
[25] A. Kokalj, J. Mol. Graphics Model. **17**, 176 (1999).
[26] P. Blaha, K. Schwarz, G. K. H. Madsen, D. Kvasnicka, and J. Luitz, *WIEN2k, An Augmented Plane Wave Plus Local Orbitals Program for Calculating Crystal Properties* (Karlheinz Schwarz, Technische Universitaet Wien, Wien, Austria, 2001).
[27] P. Rourke and S. Julian, Comput. Phys. Commun. **183**, 324 (2012).
[28] J. Rodríguez-Carvajal, Physica B **192**, 55 (1993).
[29] R. Chen, H. C. Po, J. B. Neaton, and A. Vishwanath, Nat. Phys. **14**, 55 (2018).
[30] D. Hsieh, Y. Xia, D. Qian, L. Wray, J. Dil, F. Meier, J. Osterwalder, L. Patthey, J. Checkelsky, N. P. Ong *et al.*, Nature (London) **460**, 1101 (2009).
[31] M. Matin, R. Mondal, N. Barman, A. Thamizhavel, and S. K. Dhar, Phys. Rev. B **97**, 205130 (2018).
[32] R. Mondal, S. Sasmal, R. Kulkarni, A. Maurya, A. Nakamura, D. Aoki, H. Harima, and A. Thamizhavel, Phys. Rev. B **102**, 115158 (2020).
[33] L. P. He, X. C. Hong, J. K. Dong, J. Pan, Z. Zhang, J. Zhang, and S. Y. Li, Phys. Rev. Lett. **113**, 246402 (2014).
[34] N. Kumar, K. Manna, Y. Qi, S.-C. Wu, L. Wang, B. Yan, C. Felser, and C. Shekhar, Phys. Rev. B **95**, 121109(R) (2017).
[35] J. Hu, Z. Tang, J. Liu, X. Liu, Y. Zhu, D. Graf, K. Myhro, S. Tran, C. N. Lau, J. Wei *et al.*, Phys. Rev. Lett. **117**, 016602 (2016).
[36] J. Hu, Z. Tang, J. Liu, Y. Zhu, J. Wei, and Z. Mao, Phys. Rev. B **96**, 045127 (2017).
[37] J. Du, H. Wang, Q. Chen, Q. Mao, R. Khan, B. Xu, Y. Zhou, Y. Zhang, J. Yang, B. Chen *et al.*, Sci. China: Phys. Mech. Astron. **59**, 657406 (2016).
[38] W. Gao, N. Hao, F.-W. Zheng, W. Ning, M. Wu, X. Zhu, G. Zheng, J. Zhang, J. Lu, H. Zhang *et al.*, Phys. Rev. Lett. **118**, 256601 (2017).
[39] T. A. Butcher, J. Hornung, T. Förster, M. Uhlarz, J. Klotz, I. Sheikin, J. Wosnitza, and D. Kaczorowski, Phys. Rev. B **99**, 245112 (2019).

[40] F. Wu, C. Guo, M. Smidman, J. Zhang, Y. Chen, J. Singleton, and H. Yuan, npj Quantum Mater. **4**, 20 (2019).

[41] R. Singha, B. Satpati, and P. Mandal, Sci. Rep. **7**, 6321 (2017).

[42] M. Inamdar, M. Kriegisch, L. Shafeek, A. Sidorenko, H. Müller, A. Prokofiev, P. Blaha, and S. Paschen, Solid State Phenom. **194**, 88 (2013).

[43] B. Chen, X. Duan, H. Wang, J. Du, Y. Zhou, C. Xu, Y. Zhang, L. Zhang, M. Wei, Z. Xia *et al.*, npj Quantum Mater. **3**, 40 (2018).